Transient sensitivity analysis and topology optimization of particle suspended in transient laminar fluid

Gil Ho Yoon

School of Mechanical Engineering, Hanyang University, Seoul, South Korea

Abstract

This study develops a new topology optimization scheme using coupled forward and coupled sensitivity analyses to manipulate and control time-varying particle trajectories in transient laminar flow, that is transient fluid–particle assemblies. It is an important scientific and engineering subject to manipulate or control the trajectories of particles by the drag force in steady-state or transient fluids. The drag force varies with the material properties of fluid, and the velocity differences between fluid and particles cause the particles to move. Despite some research regarding the shape and topological optimization frameworks for particles in steady-state flow, the optimization of transient particle motion in transient laminar flow is still a difficult subject. Thus, this study presents a new topology optimization scheme that considers the transient motion of particles in transient laminar flow. Owing to the time variation in the direction and magnitude of the fluid, the optimization of particle motion requires a new development of the transient sensitivity analysis. For efficient optimization, a two-scale time integration scheme for the fluid and particle was developed. The developed coupled analysis and optimization framework were applied to determine optimal layouts for transient fluids and particles. Several optimization problems were formulated and solved to validate the present scheme.

1. Introduction

This study presents a new development of a transient topology optimization scheme for the optimal trajectory of particles suspended in transient laminar flow without considering the particle–particle and particle–wall contacts. In some scientific research on microfluids, MEMS, and biology, the control and manipulation of particles in carrier fluids have been important subjects. Using the differences in the viscous force and the inertia force of a moving particle, it is possible to separate particles based on their masses and manipulate the trajectories of particles. With the help of additional forces, it is also possible to enhance the flexibility and controllability of control device. Several relevant studies exist on topology optimization for this subject under laminar flow conditions [1–3]. To contribute to this research area, this study considers the topology optimization problem of particles in a transient laminar flow. With the solid isotropic material with penalization (SIMP) method for the interpolation of Darcy force regarding the spatially varying design variables, some optimal topologies defining pseudo rigid bodies can be found in transient laminar flow (Fig. 1).

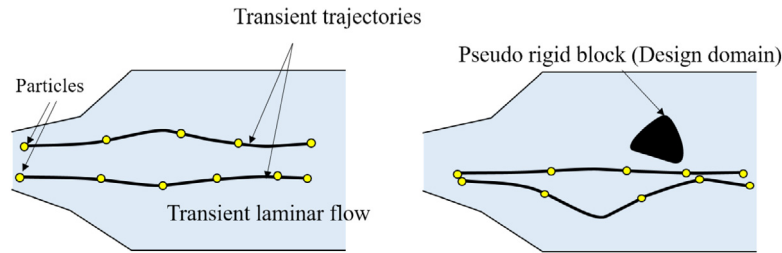*E-mail address:* ghy@hanyang.ac.kr.

Fig. 1. Topology optimization of particles in transient laminar flow.

After the introduction of the structural topology optimization scheme, various optimization schemes have been studied and applied to various engineering applications (see [4–7] and references therein). In the beginning, the homogenization-based topology optimization scheme and its variations were studied for application in structural optimization[4]. The explicit or implicit level-set approach was also an actively researched topic in structural optimization [5,7]. The MMC (Moving Morphable Component) and MMV (Moving Morphable Void) approaches were also actively studied in structural optimization [6]. As the topology optimization scheme can determine optimal layouts without an initial design, it was applied to multiphysics systems whose layouts were difficult to design by engineers [8–11]. Recently, the application of this optimization to fluids has been extensively studied. Topology optimization schemes for turbulent fluids have also been studied recently [8,9,12]. Transient sensitivity analysis and topology optimization for time-varying flow problems were formulated and presented (see [11] for rigorous sensitivity analysis and topology optimization scheme). The multiphysics system of the conjugate heat transfer problem was also considered (see [10,13–15] and references therein). A sophisticated review of the structural optimization of the heat and fluid coupled system can be found in [15]. Some relevant studies regarding structural topology optimization of the trajectory of particles in steady-state laminar fluid have been proposed recently [1–3,16–18]. This study extends these works to consider the transient trajectory of particles in a transient laminar flow [1].

Controlling small particles in a fluid is considered a difficult subject from both theoretical and practical perspectives. It is an innovative approach to apply external forces, such as electrostatic and electromagnetic forces, and hydrodynamic effects, to deliberately manipulate the trajectory of particles [19–24]. In [19], the optimization of an electrokinetic micromixer was proposed. By alternating the electric potential, the electrokinetic flow was used to enhance the mixing of the concentrated species. Several innovative numerical approaches were proposed to efficiently analyze the transient trajectory of particles [21,25–27]. In [20], a direct staggered simulation of the fluid and particles was proposed. To consider mutual coupling, the fluid mesh was automatically updated according to the position of the particle. In [28], the CFD–DEM coupled simulation was conducted, considering the drag and buoyancy forces. The positions of particles and the size and rotation effects of particles on steady-state or transient fluid were considered and analyzed in fluid–particle assemblies. To simplify the computation, it is often useful to adopt a one-way coupling approach assuming a small particle condition, neglecting the rotation. In other words, the effect of particles on the fluid and the effect of the rotations of particles were neglected to simplify the simulation process. [21,25–27,29–32]. This one-way coupling approach is also important for simplifying the forward and sensitivity analyses (Refer [2] for the example of the sensitivity derivation). This one-way coupled multiphysics equation can be an effective approach for analyzing fluid and particle interaction simulations. Note that this study presents the topology optimization formulation with the assumption of the small particle and the one-way coupling. This means that the rotation of the particle and lift force are not considered in the present formulation.

This study considers the application of a topology optimization scheme that considers the transient fluid flow [1–3]. As studied in the steady-state Navier–Stokes equation, Darcy forces interpolated with spatially varying design variables are added to the transient Navier–Stokes equation [1–3]. As the contact simulation among particles and the wall increases the complexities, this study does not consider the contact condition. By modifying the multiphysics equations (Navier–Stokes equation and Newton's second law of motion) and deriving the transient sensitivity analysis for the trajectory of a particle, the optimal distributions of porous media or pseudo rigid bodies can be determined. One of the numerical difficulties is the time scale difference between the fluid and the particle. A two-time scale integration scheme is also developed for efficient forward analysis and efficient sensitivity analysis. With these developed ideas and schemes, an optimization formulation is proposed and solved. We believe that the

schemes and the presented results are promising and pave the way for more challenging applications related to the particle problem in fluid.

The article is organized as follows: Section 2 provides a background pertaining to the coupled analysis of particle and transient fluid motion and the development of the transient sensitivity analysis of the objective function formulated with particle trajectory. In addition, a two-time scale scheme was developed for efficient transient sensitivity analysis. Section 3 describes several topology optimization formulations and results. Section 4 presents the conclusions and provides suggestions for future research.

2. Transient multiphysics analysis and optimization formulation

This section describes the development of the topology optimization scheme and the multiphysics analysis coupling between the transient Navier–Stokes equation and Newton's second law of a particle. The finite element procedure was implemented to analyze the transient laminar flow without the loss of generality, and the Newmark scheme was implemented for the transient analysis of particles. The objective and constraints formulated and considered here were mainly set as functions of the final positions of particles [1]. To model the pseudo rigid domain in the fluid, the pseudo-Darcy force was added to the transient Navier–Stokes equation. In addition, the transient sensitivity analysis of the particle position was presented and investigated. To accelerate the computational procedure, a two-time scale analysis approach for the coupling analysis of transient fluid and particle was also developed.

2.1. Transient fluid equation and particle equation

This study advances the effort made to consider and optimize the positions of particles in coordination with the topology optimization scheme. To simulate the transient motion of particles in fluid, some numerical schemes already exist (see [1,2,16–18,24] and references therein for mathematical theory and applications). This study assumes that the particle size is sufficiently small and does not affect the fluid viscosity and consequently the motion of the fluid. It has been revealed that with relatively large particles or external forces, the consideration of particle size is necessary. For fluid topology optimization, the transient laminar Navier–Stokes equation is solved with the Darcy force, $\alpha \mathbf{u}$. With a sufficiently large α, the corresponding regions are modeled as pseudo rigid domains with sufficiently small velocity.

$$\rho \frac{\partial \mathbf{u}}{\partial t} + \rho(\mathbf{u} \cdot \nabla)\mathbf{u} = \nabla \cdot \left[-p\mathbf{I} + \mu(\nabla\mathbf{u} + \nabla\mathbf{u}^{\mathrm{T}})\right] - \alpha\mathbf{u} \quad \text{on} \quad \Omega$$
$$\nabla \cdot \mathbf{u} = 0 \tag{1}$$

The fluid domain is denoted by Ω, as previously mentioned. To model the pseudo rigid domain with the spatially varying design variables, the Darcy force with the SIMP method was formulated.

$$\alpha = \alpha_{max}\boldsymbol{\gamma}^n \tag{2}$$

where the spatial varying design variables defining pseudo rigid domain are denoted by $\boldsymbol{\gamma}$. At the end of the transient Navier–Stokes equation in Eq. (1), the Darcy force was added. For structural topology optimization, the SIMP model is adopted with penalization n in this study [1–3,11,16,18,30,31]. The following boundary conditions were imposed:

$$\begin{aligned}
&\text{Time varying inflow or outflow b.c.: } \mathbf{u} = \mathbf{u}^*(t) \quad \text{on} \quad \Gamma_{u*} \\
&\text{No-slip b.c.: } \mathbf{u} = \mathbf{0} \quad \text{on} \quad \Gamma_{u0} \\
&\text{Pressure b.c.: } \left[-p\mathbf{I} + \mu(\nabla\mathbf{u} + \nabla\mathbf{u}^{\mathrm{T}})\right] \cdot \mathbf{n} = p_p\mathbf{n} \quad \text{on} \quad \Gamma_p^*
\end{aligned} \tag{3}$$

The velocity, pressure, mass density, and dynamic viscosity are denoted by $\mathbf{u}$, p, ρ, and μ, respectively. The boundary conditions are described by either the fluid velocity condition (no-slip boundary condition along Γ_{u0}, the inflow/outflow boundary condition along $\boldsymbol{\Gamma_u^*}$) or the pressure boundary condition along Γ_p^*.

The Newton's second law can be numerically solved using the fluid drag force as follows:

$$\frac{d}{dt}(m_p\mathbf{v}) = m_p F_D(\mathbf{u} - \mathbf{v}), \quad \frac{d\mathbf{x}}{dt} = \mathbf{v} \tag{4}$$

$$F_D = \frac{18\mu}{\rho_p d_p^2} \tag{5}$$

where the drag force coefficient is denoted by F_D. In the above formulations, the diameter, mass, density, and velocity of a particle are denoted by d_p, m_p, ρ_p, and $\mathbf{v}$, respectively. The coordinates of the particle are set to $\mathbf{x}$. In addition, in the above formulations, the fluid velocities are time-varying terms, and the drag force with these time-varying fluid velocities is also a time-varying term. In the drag force in (4), the proportional constant is $m_p F_D$. Therefore, the direction of the drag force is naturally opposite to the direction of the relative motion of the particle to the fluid. To determine and model the drag force, some innovative experimental and theoretical models have been presented [20, 24,33–35]. To solve the transient Navier–Stokes equation, the quadratic interpolation functions for the velocity and the linear interpolation functions for the pressure are implemented in the framework of Matlab. The stabilization scheme is not used here. The Newmark scheme is a solver for particle motion (Beta = 1/6, Gamma = 1/3).

2.2. Adjoint sensitivity analysis of the transient trajectory of particle

The main objective of the optimization problem is to manipulate the loci of particles considering the transient fluid. Through topology optimization, this study aims to determine an optimized layout that increases the control capability of a device. To achieve this, several conditions are assumed. The first assumed condition is a transient laminar flow. In a steady-state laminar flow, spatial variations in fluid velocities were observed, and they were not time-varying terms. In a transient laminar flow, the fluid velocities vary in time and location. Particles can move across, migrate, and follow streamlines, and the transient motions occur. Thus, more complex motions of the particles were observed. Depending on the properties of the particles from an inertial point of view, they show different loci. These differences apply to the control of the particles. Transient forward analysis was performed to determine the positions of the particles. Transient sensitivity analysis was performed for optimization. As the contact simulation between particle and particle and particle–wall increase the numerical complexities, the contact conditions are ignored. We believe that commonly used contact theories should be modified for structural topology optimization. The objective function or the final position, $\mathbf{x}_f$, is formulated using the position vector.

$$\text{Final position of particle: } \mathbf{x}_f = \int_0^{t_f} \mathbf{x}\delta(t = t_f)dt \tag{6}$$

The objective function is set as a function of the final position with the Dirac delta. The Lagrangian $\mathbf{L}$ over a period should be defined by considering the position, velocity, and acceleration of the particle; the transient fluid velocity; and the fluid acceleration as follows:

$$\mathbf{L} = \int_0^{t_f} \mathbf{c}(\mathbf{x}, \dot{\mathbf{x}}, \ddot{\mathbf{x}})dt + \int_0^{t_f} \boldsymbol{\lambda}^T(\mathbf{M}\ddot{\mathbf{x}} - \mathbf{F}(\dot{\mathbf{x}}, \mathbf{u}))dt + \int_0^{t_f} \boldsymbol{\psi}^T \underbrace{(\mathbf{E}\dot{\mathbf{u}} + \mathbf{R}(\mathbf{u}, \boldsymbol{\gamma}))}_{\mathbf{S}(\mathbf{u}, \dot{\mathbf{u}}, \boldsymbol{\gamma})}dt \tag{7}$$

where the general objective function depending on the position, velocity, and acceleration of the particle is denoted by $\mathbf{c}$. The simulation time is denoted by t_f. The Lagrange multipliers are denoted by $\boldsymbol{\lambda}$ and $\boldsymbol{\psi}$. For convenience, the equations of the fluid are set to $\mathbf{S} = \mathbf{0}$.

The objective function is formulated as a vector quantity, rather than a scalar quantity, to consider the location vectors of the particles. For the sensitivity, the following differentiation of the Lagrangian is then obtained about the design variable, γ_e which is the design variable of the eth element.

$$\begin{aligned}
\frac{\partial \mathbf{L}}{\partial \gamma_e} &= \int_0^{t_f} \left(\frac{\partial \mathbf{c}}{\partial \mathbf{x}}\frac{\partial \mathbf{x}}{\partial \gamma_e} + \frac{\partial \mathbf{c}}{\partial \dot{\mathbf{x}}}\frac{\partial \dot{\mathbf{x}}}{\partial \gamma_e} + \frac{\partial \mathbf{c}}{\partial \ddot{\mathbf{x}}}\frac{\partial \ddot{\mathbf{x}}}{\partial \gamma_e} \right) dt + \int_0^{t_f} \boldsymbol{\lambda}^T \left(\mathbf{M}\frac{\partial \ddot{\mathbf{x}}}{\partial \gamma_e} - \frac{\partial \mathbf{F}}{\partial \dot{\mathbf{x}}}\frac{\partial \dot{\mathbf{x}}}{\partial \gamma_e} - \frac{\partial \mathbf{F}}{\partial \mathbf{u}}\frac{\partial \mathbf{u}}{\partial \gamma_e} \right) dt \\
&+ \int_0^{t_f} \boldsymbol{\psi}^T \left(\frac{\partial \mathbf{S}}{\partial \dot{\mathbf{u}}}\frac{\partial \dot{\mathbf{u}}}{\partial \gamma_e} + \frac{\partial \mathbf{S}}{\partial \mathbf{u}}\frac{\partial \mathbf{u}}{\partial \gamma_e} + \frac{\partial \mathbf{S}}{\partial \gamma_e} \right) dt,
\end{aligned} \tag{8}$$

where the first integration of the right side is the differentiation of the objective function using the chain rule, and the second and third integration parts correspond to the differentiation of the particle equation and the transient fluid equation, respectively. To obtain the two adjoint equations for the Lagrange multipliers $\boldsymbol{\lambda}$ and $\boldsymbol{\psi}$, the integration by parts for the acceleration and the velocities should be considered as follows:

$$\begin{aligned}
\text{Acceleration: } \int_0^{t_f} \boldsymbol{\lambda}^T\mathbf{M}\frac{\partial \ddot{\mathbf{x}}}{\partial \gamma_e}dt &= -\int_0^{t_f} \frac{d\boldsymbol{\lambda}^T}{dt}\mathbf{M}\frac{\partial \dot{\mathbf{x}}}{\partial \gamma_e}dt + \left(\left(\boldsymbol{\lambda}^T\mathbf{M}\frac{\partial \dot{\mathbf{x}}}{\partial \gamma_e} \right)\bigg|_0^{t_f} \right) \\
&= \int_0^{t_f} \frac{d^2\boldsymbol{\lambda}^T}{dt^2}\mathbf{M}\frac{\partial \mathbf{x}}{\partial \gamma_e}dt - \left(\left(\frac{d\boldsymbol{\lambda}^T}{dt}\mathbf{M}\frac{\partial \mathbf{x}}{\partial \gamma_e} \right)\bigg|_0^{t_f} \right) + \left(\left(\boldsymbol{\lambda}^T\mathbf{M}\frac{\partial \dot{\mathbf{x}}}{\partial \gamma_e} \right)\bigg|_0^{t_f} \right)
\end{aligned} \tag{9}$$

To transform the acceleration and the velocity of a particle into the differentiation of position, the differentiation by parts was applied. Assuming zero displacement and velocity of the Lagrange multiplier, $\boldsymbol{\lambda}$, the last two parts of the last right side can be set to zero at $t = t_f$. The differentiation of Darcy force $\mathbf{F}$ was then transformed similarly as follows:

$$\int_0^{t_f} \boldsymbol{\lambda}^{\mathrm{T}} \left(-\frac{\partial \mathbf{F}}{\partial \dot{\mathbf{x}}} \frac{\partial \dot{\mathbf{x}}}{\partial \gamma_e} \right) dt = -\int_0^{t_f} \frac{d\boldsymbol{\lambda}^{\mathrm{T}}}{dt} \left(-\frac{\partial \mathbf{F}}{\partial \dot{\mathbf{x}}} \frac{\partial \mathbf{x}}{\partial \gamma_e} \right) dt + \left(-\boldsymbol{\lambda}^{\mathrm{T}} \frac{\partial \mathbf{F}}{\partial \dot{\mathbf{x}}} \frac{\partial \mathbf{x}}{\partial \gamma_e} \Big|_0^{t_f} \right),$$
$$\boldsymbol{\lambda} = \mathbf{0}, \quad \frac{\partial \boldsymbol{\lambda}}{dt} = \mathbf{0}, \text{ at } t = t_f, \tag{10}$$

Similar to the above integration by parts, the differentiation of $\mathbf{S}$ can be transformed into the following form:

$$\int_0^{t_f} \boldsymbol{\psi}^{\mathrm{T}} \frac{\partial \mathbf{S}}{\partial \dot{\mathbf{u}}} \frac{\partial \dot{\mathbf{u}}}{\partial \gamma_e} dt = -\int_0^{t_f} \frac{d\boldsymbol{\psi}^{\mathrm{T}}}{dt} \frac{\partial \mathbf{S}}{\partial \dot{\mathbf{u}}} \frac{\partial \mathbf{u}}{\partial \gamma_e} dt + \left(\left(\boldsymbol{\psi}^{\mathrm{T}} \frac{\partial \mathbf{S}}{\partial \dot{\mathbf{u}}} \frac{\partial \mathbf{u}}{\partial \gamma_e} \right) \Big|_0^{t_f} \right),$$
$$\boldsymbol{\psi} = \mathbf{0}, \quad \text{at } t = t_f \tag{11}$$

By substituting the above formula into the differentiation of the Lagrange multiplier, $\mathbf{L}$, the following can be obtained:

$$\begin{aligned}
\frac{\partial \mathbf{L}}{\partial \gamma_e} &= \int_0^{t_f} \left(\frac{\partial \mathbf{c}}{\partial \mathbf{x}} \frac{\partial \mathbf{x}}{\partial \gamma_e} - \frac{d}{dt} \frac{\partial \mathbf{c}}{\partial \dot{\mathbf{x}}} \frac{\partial \mathbf{x}}{\partial \gamma_e} + \frac{d^2}{dt^2} \frac{\partial \mathbf{c}}{\partial \ddot{\mathbf{x}}} \frac{\partial \mathbf{x}}{\partial \gamma_e} \right) dt \\
&+ \int_0^{t_f} \frac{d^2 \boldsymbol{\lambda}^{\mathrm{T}}}{dt^2} \mathbf{M} \frac{\partial \mathbf{x}}{\partial \gamma_e} - \frac{d\boldsymbol{\lambda}^{\mathrm{T}}}{dt} \left(-\frac{\partial \mathbf{F}}{\partial \dot{\mathbf{x}}} \frac{\partial \mathbf{x}}{\partial \gamma_e} \right) - \boldsymbol{\lambda}^{\mathrm{T}} \frac{\partial \mathbf{F}}{\partial \mathbf{u}} \frac{\partial \mathbf{u}}{\partial \gamma_e} dt \\
&+ \int_0^{t_f} -\frac{d\boldsymbol{\psi}^{\mathrm{T}}}{dt} \frac{\partial \mathbf{S}}{\partial \dot{\mathbf{u}}} \frac{\partial \mathbf{u}}{\partial \gamma_e} + \boldsymbol{\psi}^{\mathrm{T}} \left(\frac{\partial \mathbf{S}}{\partial \mathbf{u}} \frac{\partial \mathbf{u}}{\partial \gamma_e} + \frac{\partial \mathbf{S}}{\partial \gamma_e} \right) dt \\
&= \int_0^{t_f} \boldsymbol{\psi}^{\mathrm{T}} \left(\frac{\partial \mathbf{S}}{\partial \gamma_e} \right) dt + \int_0^{t_f} \left(\begin{matrix} \left(\frac{d^2}{dt^2} \frac{\partial \mathbf{c}}{\partial \ddot{\mathbf{x}}} - \frac{d}{dt} \frac{\partial \mathbf{c}}{\partial \dot{\mathbf{x}}} + \frac{\partial \mathbf{c}}{\partial \mathbf{x}} \right) \frac{\partial \mathbf{x}}{\partial \gamma_e} + \left(\frac{d^2 \boldsymbol{\lambda}^{\mathrm{T}}}{dt^2} \mathbf{M} + \frac{d\boldsymbol{\lambda}^{\mathrm{T}}}{dt} \frac{\partial \mathbf{F}}{\partial \dot{\mathbf{x}}} \right) \frac{\partial \mathbf{x}}{\partial \gamma_e} \\ \left(-\boldsymbol{\lambda}^{\mathrm{T}} \frac{\partial \mathbf{F}}{\partial \mathbf{u}} - \frac{d\boldsymbol{\psi}^{\mathrm{T}}}{dt} \frac{\partial \mathbf{S}}{\partial \dot{\mathbf{u}}} + \boldsymbol{\psi}^{\mathrm{T}} \frac{\partial \mathbf{S}}{\partial \mathbf{u}} \right) \frac{\partial \mathbf{u}}{\partial \gamma_e} \end{matrix} \right) dt \\
&= \int_0^{t_f} \boldsymbol{\psi}^{\mathrm{T}} \left(\frac{\partial \mathbf{S}}{\partial \gamma_e} \right) dt
\end{aligned} \tag{12}$$

To remove the coefficient equations for $\frac{\partial \mathbf{x}}{\partial \gamma_e}$ and $\frac{\partial \mathbf{u}}{\partial \gamma_e}$, the corresponding factors were set to zero, and the following adjoint equations were obtained for the Lagrange multipliers. The first adjoint equation was formulated for the Lagrange multiplier $\boldsymbol{\lambda}$ as follows:

$$\text{Adjoint 1}: \frac{d^2 \boldsymbol{\lambda}^{\mathrm{T}}}{dt^2} \mathbf{M} + \frac{d\boldsymbol{\lambda}^{\mathrm{T}}}{dt} \frac{\partial \mathbf{F}}{\partial \dot{\mathbf{x}}} = -\left(\frac{d^2}{dt^2} \frac{\partial \mathbf{c}}{\partial \ddot{\mathbf{x}}} - \frac{d}{dt} \frac{\partial \mathbf{c}}{\partial \dot{\mathbf{x}}} + \frac{\partial \mathbf{c}}{\partial \mathbf{x}} \right)$$
$$\boldsymbol{\lambda} = \mathbf{0}, \quad \frac{\partial \boldsymbol{\lambda}}{dt} = \mathbf{0}, \text{ at } t = t_f, \tag{13}$$

Notably, the adjoint equation shares a similarity with the equation of motion of the particle with damping, $\frac{\partial \mathbf{F}}{\partial \dot{\mathbf{x}}}$, and the time-varying force depends on the location. The second adjoint equation is formulated as follows:

$$\text{Adjoint 2}: -\boldsymbol{\lambda}^{\mathrm{T}} \frac{\partial \mathbf{F}}{\partial \mathbf{u}} - \frac{d\boldsymbol{\psi}^{\mathrm{T}}}{\partial \mathbf{F}} \partial \dot{\mathbf{u}} + \boldsymbol{\psi}^{\mathrm{T}} \frac{\partial \mathbf{S}}{\partial \mathbf{u}} = \mathbf{0},$$
$$\boldsymbol{\psi} = \mathbf{0}, \quad \text{at } t = t_f \tag{14}$$

The equation is also similar to the transient fluid equation, and the term $\frac{\partial \mathbf{S}}{\partial \mathbf{u}}$ is the tangent stiffness matrix. To solve the above adjoint equations, a time-reversal scheme should be adopted. For the rigorous derivations of the sensitivity values, the above formulations are based on the position vector of the particle. For the optimization process, the component of the location of the particle in (6) was considered the objective value, that is, the x-position or the y-position.

Two scale time integration scheme for particle and transient fluid

The finalized sensitivity analysis of the particles can be written as follows:

$$\frac{\partial \mathbf{L}}{\partial \gamma_e} = \int_0^{t_f} \boldsymbol{\psi}^{\mathrm{T}} \left(\frac{\partial \mathbf{S}}{\partial \gamma_e} \right) dt \tag{15}$$

The Newmark scheme was used for the particle equation, and the backward differentiation formulation was used for the Navier–Stokes equation. In our numerical implementation, the two-scale time-stepping approach adopting the different time steps for the Newmark scheme and the backward differentiation formulation was developed. In other words, a relatively small time step was used for the particle solver to obtain a stable and nonoscillating solution for the particle. Conversely, a relatively large time step was used for the transient fluid solver. We assume that the time variation of the fluid was smaller than that of the particle. In addition, as the instabilities of the particle loci were observed with a larger time step, a very small time step was necessary for the particle equation. Therefore, the multiscale time integration scheme can accelerate the computational procedure. With the present multiscale time step algorithm, the above forward and sensitivity analyses were computed with different time scales as follows:

$$\text{Time scale for particle: } t = [0 : \Delta t_m : t_f], \mathbf{M}\ddot{\mathbf{x}} - \mathbf{F}(\dot{\mathbf{x}}, \mathbf{u}) = \mathbf{0} \tag{16}$$

$$\text{Time scale for fluid: } t = [0 : \Delta t_f : t_f], \mathbf{E}\dot{\mathbf{u}} + \mathbf{R}(\mathbf{u}, \boldsymbol{\gamma}) = \mathbf{0} \tag{17}$$

where Δt_m and Δt_f denote the time step of the particle and the time step of the fluid, respectively. In this study, the time steps were set as $\Delta t_f > \Delta t_m$. After calculating the transient fluid motion, the fluid velocities were used to calculate the drag force, $\mathbf{F}(\dot{\mathbf{x}}, \mathbf{u})$. Notably, with $\Delta t_f = \Delta t_m$, the corresponding fluid velocities at the time of interest can be used without any complications. However, with different time steps, an interpolation scheme is required. In our implementation, a simple linear interpolation of the fluid velocities was used. For example, to compute the drag force at $t = k\Delta t_m$ ($k = 0, 1, 2, \ldots \frac{t_f}{\Delta t_m}$), the adjacent fluid times, t_1^{adjacent} and t_2^{adjacent}, which include $t = k\Delta t_m$, were first found using a sorting algorithm.

$$t = k\Delta t_m, \ k = 0, 1, 2, \ldots, \frac{t_f}{\Delta t_m},$$
$$t_1^{\text{adjacent}} \le k\Delta t_m \le t_2^{\text{adjacent}} \tag{18}$$

To determine the interpolated fluid velocity for $\mathbf{F}(\dot{\mathbf{x}}, \mathbf{u})$, the fluid velocities at the times are defined as follows:

$$\mathbf{u}_{t_1^{\text{adjacent}}} = \mathbf{u}(t = t_1^{\text{adjacent}}), \ \mathbf{u}_{t_2^{\text{adjacent}}} = \mathbf{u}(t = t_2^{\text{adjacent}}) \tag{19}$$

Then, the following drag forces can be defined at time $t = k\Delta t_m$ for particle simulation.

$$\mathbf{F}(\dot{\mathbf{x}}, \mathbf{u})|_{t=k\Delta t_m} = m_p F_D(\mathbf{u} - \dot{\mathbf{x}})\big|_{t=k\Delta t_m}, \tag{20}$$

The fluid velocities at $t = k\Delta t_m$ were linearly interpolated as follows:

$$\mathbf{u}|_{t=k\Delta t_m} = \frac{\mathbf{u}_{t_2}^{\text{adjacent}} - \mathbf{u}_{t_1}^{\text{adjacent}}}{\Delta t_f} \times \left(k\Delta t_m - t_1^{\text{adjacent}} \right) + \mathbf{u}_{t_1}^{\text{adjacent}} \tag{21}$$

Fig. 2 shows the concept of the interpolated fluid velocities for the time, at which the particle force is computed. The above linear interpolation scheme was also applied to for the first Lagrange multiplier, $\boldsymbol{\lambda}$, in the second adjoint equation, i.e., $\boldsymbol{\lambda}^{\mathrm{T}} \frac{\partial \mathbf{F}}{\partial \mathbf{u}}$. The final sensitivity in (15) was also integrated with the fluid time interval, i.e., Δt_f. This approach improves the computational efficiency and also saves the memory usages. The analysis and the optimization procedures were implemented in Matlab.

3. Numerical examples

To demonstrate the application of this development, this section presents the optimization formulation and optimized layouts controlling the transient trajectories of particles suspended in transient fluid. The objective and some constraints of the optimization problems were formulated based on the positions of the particles. It is possible to apply the existing filter schemes to impose the manufacturing constraint or remove the checkerboard pattern. As this study intends to show the optimization for particles suspended in transient fluid, the optimization results
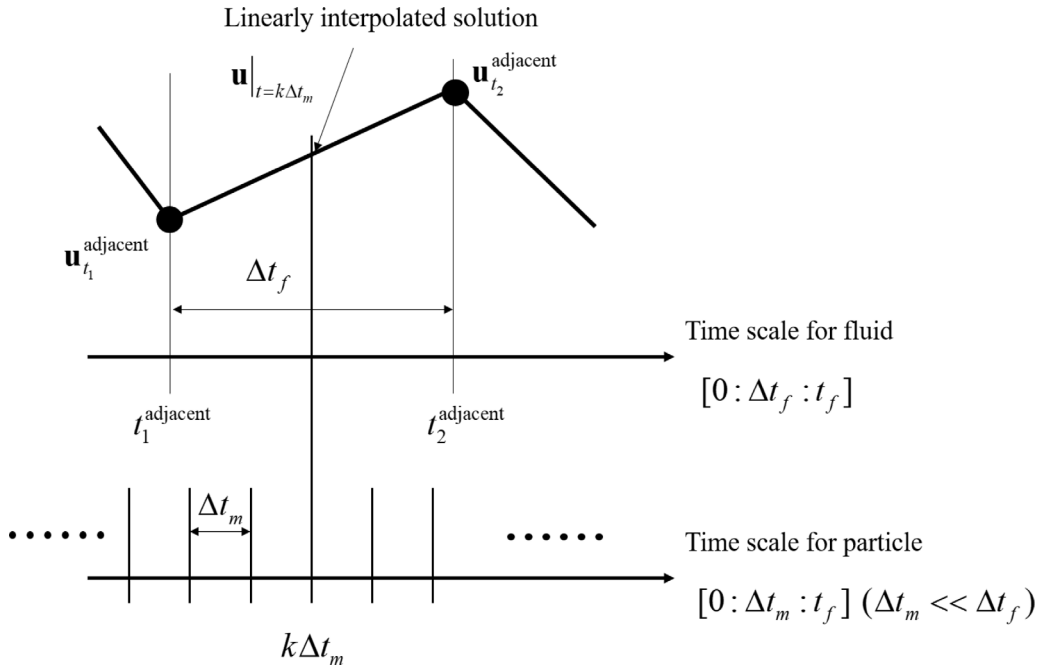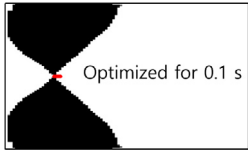
Fig. 2. Two time scale method.

Table 1
Reevaluations of the first optimization design (the value with *: the best objective function in the analysis conditions).

Design	Analysis condition	
	Final time (0.1 s)	Final time (1 s)
Optimized for 0.1 s	1.3422×10^{-3} m *	1.0211×10^{-2} m
Optimized for 1 s	9.380×10^{-4} m	1.326×10^{-2} m*

without the filtering scheme are presented. The method of moving asymptotes (MMA) algorithm was used for an optimization algorithm [36]. From our numerical experiments, optimized layouts for the fluid-based optimization with the pseudo rigid domain are highly affected by the maximum permeability in (1). As the optimization problems are nonconvex, the presented optimized layouts are the local optima.

3.1. Topology optimization example 1: Accelerating particle

For the first example, the topology optimization accelerating a particle with a diameter of 4 μm is considered in Fig. 3. Initially the particle is standing still. The objective is set to the final position of the particle, and the mass

(a)

(b)

(c)

(d)

(e)
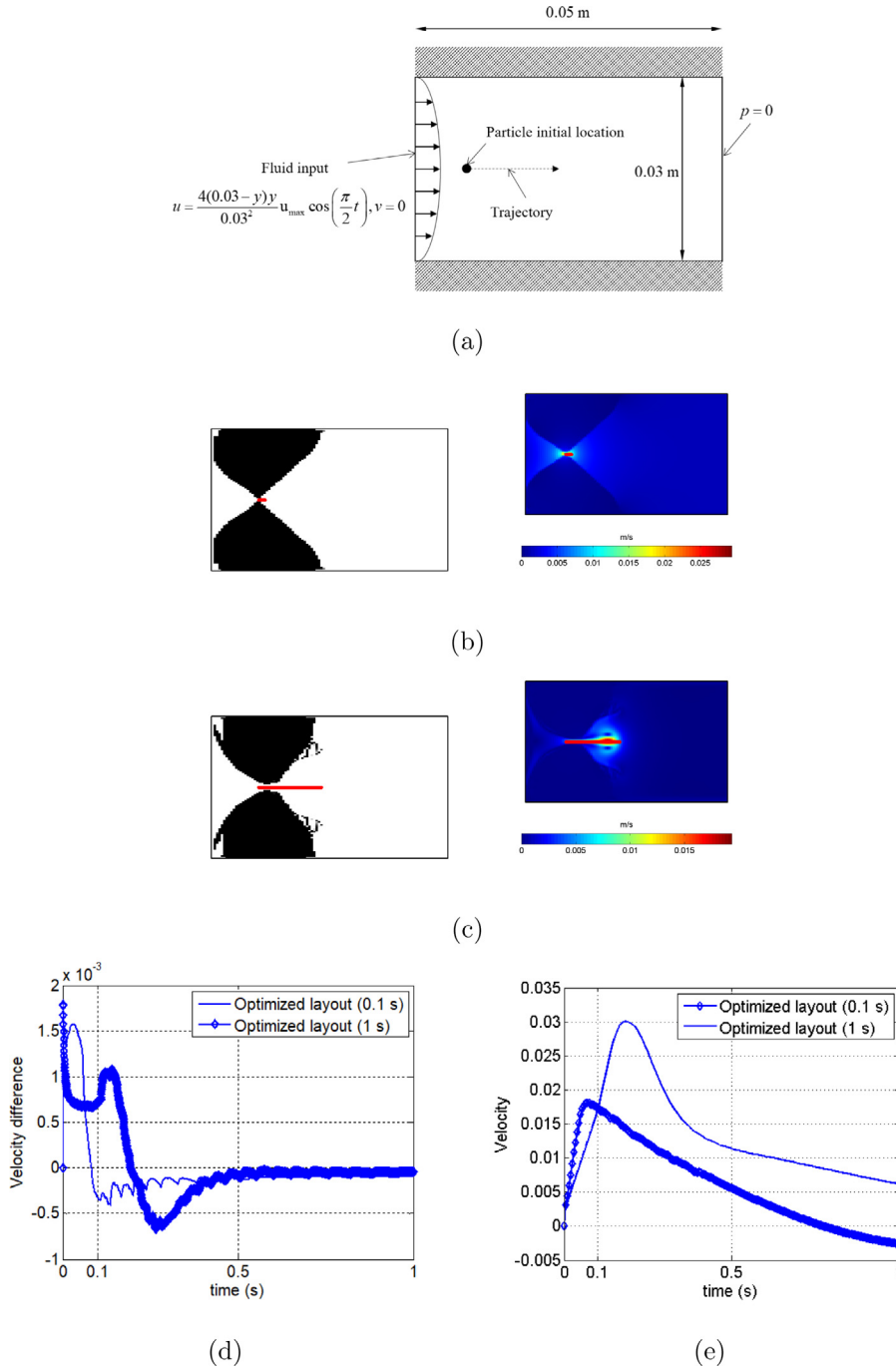
Fig. 3. Example 1: A channel design to accelerate the particle. (a) The problem definition (Initial locations: (1 cm, 1.5 cm), $u_{max} = 0.01$ m/s, Fluid material property : density= 1000 kg/m^3, dynamic viscosity= 352×10^{-6} Pa×s, Particle property: mass= 6.367×10^{-14} kg (Radius =2.00 μm, density= 1900 kg/m^3), F_D=$1.327 \times 10^{-8} \frac{\text{N·s}}{\text{kg·m}}$, mass$_0$: 30%, the design domain discretized by 80 by 80 quad elements, Δt_f= 0.01 (s), Δt_m= 5 $\times 10^{-6}$ (s)), the optimization results and the fluid velocities for 0.1 (s) in (b) and 1 (s) in (c),(d) the velocity differences ($\mathbf{u} - \mathbf{v}$) of the two designs and (e) the velocity curves of the two designs.

(a)   (b)   (c)
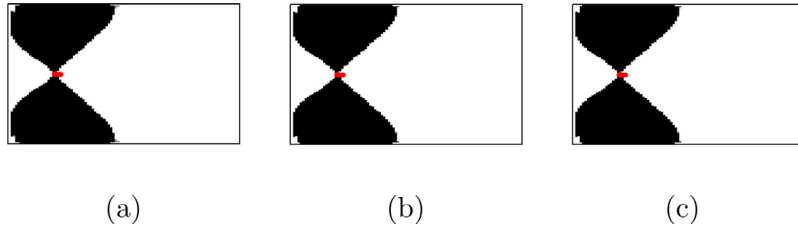
Fig. 4. Numerical tests for the time difference. The optimization results with (a) Δt_f =0.005 s, (b) Δt_f =0.02 s and (c) Δt_f =0.0001 s.

(a)

(b)
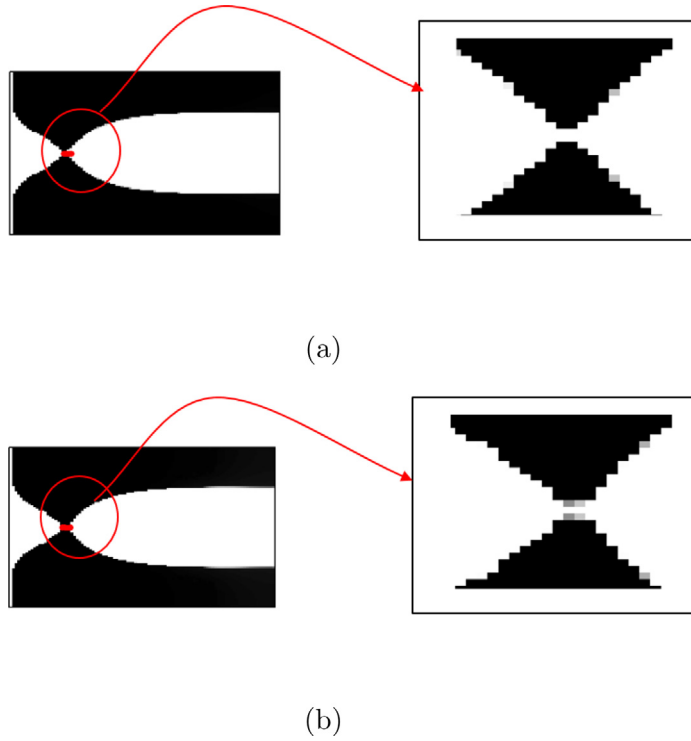
Fig. 5. Investigation of the mass constraint and the mesh effect (Δt_f =0.1 s). (a) Optimized layout without mass constraint (100 $\times$ 100 elements) and (b) optimized layout with different meshes (100 $\times$ 99 elements).

constraint (30% for the pseudo rigid domain) is considered in (22).

$$
\begin{aligned}
&\underset{\gamma}{\text{Max}} \quad p_x \\
&\text{Subject to Mass} \ \leq \text{mass}_0 \\
&\gamma = [\gamma_1, \gamma_2, \ldots, \gamma_{N_e}], \quad \gamma_{\min} \leqslant \gamma \leqslant 1, \quad \gamma_{\min} = 0.001,
\end{aligned}
\tag{22}
$$

where the design variable is denoted by γ. The lower bound of the design variable is set to 0.001; with zero, the similar layouts are obtained [37]. The position of the particle in the x-direction is denoted by p_x, and the upper bound of the mass constraint is mass$_0$. The particle is suspended in water flowing toward the right side with the transient parabolic fluid input varying in magnitude with $\cos(\frac{\pi}{2}t)$. The analysis and design domain are set to the box (0.05 m by 0.03 m). Fig. 3(b) and (c) show the optimized layouts with the 0.1 (s) and 1 (s) final times, respectively.

(a)

(b)
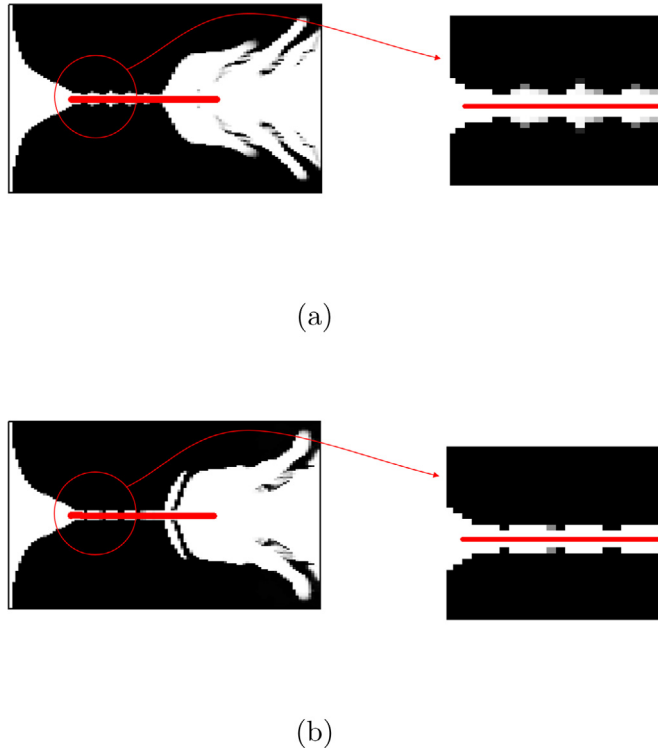
Fig. 6. Investigation of the mass constraint and the mesh effect (Δt_f =1 s). (a) Optimized layout without mass constraint (100 × 100 elements) and (b) optimized layout with different meshes (100 × 99 elements).

(a)   (b)
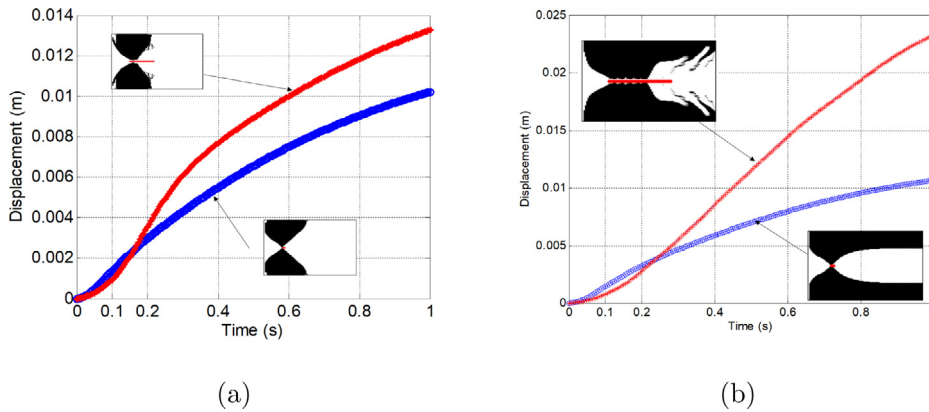
Fig. 7. (a) Comparison of the trajectories of the optimized designs in Fig. 3 and (b) a comparison of the trajectories of the optimized designs in Fig. 5(a) and Fig. 6(b).

The optimization for 0.1 (s) is to determine an optimal layout with a small fluid variation, and the optimization for 1 (s) is obtained with decreasing fluid velocity. As expected, the optimized layout shown in Fig. 3(b) mainly concentrates the fluid input to accelerate the particle for 0.1 (s). However, the design shown in Fig. 3(c), for 1 (s)
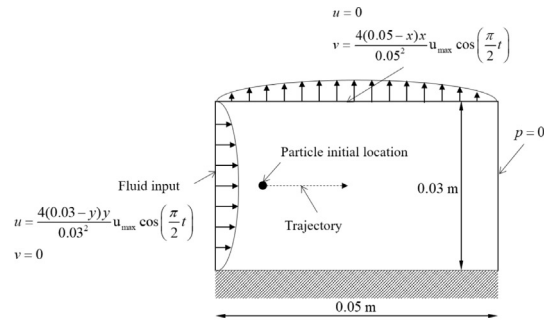
(a)
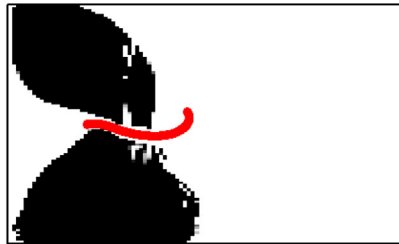
(b)

Fig. 8. Example with the different boundary condition for 1 s (Mass: 30%). (a) Boundary condition and (b) optimized layout.

shows a long narrow channel. By comparing the designs in (b) with (c), it can be seen that the parabolic fluid inlet is concentrated at the center of the design domain. The figure showing the fluid magnitude reveals that the design shown in Fig. 3(c) maintains a higher fluid velocity for a longer time. It turns out that the optimized layout and the optimized layouts with the different fluid time steps are similar to that of the stationary fluid that proves the validity of the present scheme indirectly. Table 1 compares the objective values reevaluated to check the optimality conditions for the boundary conditions. The optimized design shown in Fig. 3(b) with the fluid input for 0.1 (s) is better in the objective function compared with the optimized design in Fig. 3(c). The design in Fig. 3(c) makes the particle move far more than the design shown in Fig. 3(b), for 1 s. Fig. 3(d) shows the velocity differences $(\mathbf{u} - \mathbf{v})$ of the two designs, which are multiplied by the drag force coefficient. As expected, the design obtained with the simulation of 0.1 s accelerates primarily for 0.1 s, and the design obtained with 1 s for the final time accelerates primarily for 1 s. Fig. 3(e) shows the velocities of the optimized layouts. As illustrated, the design optimized for 0.1 s accelerates the particle further for 0.1 s than the design optimized for 1 s. Conversely, the design optimized for 1 s moves the particle further for 1 s. After release, the particles are accelerated and move in the positive x direction. Thus, a large force is applied at a few time integration steps according to Newton's second law of motion. This example shows that the present optimization framework can determine locally optimized layouts considering the transient fluid condition. Not presented here, the responses of the above designs are reanalyzed with the different particle time steps. With a sufficiently small time step, the responses were similar. An optimization investigation on the effect of particle density and drag force on the optimized layout was also conducted. When the trajectory is similar, a similar layout can be obtained for a single-particle case.

To test the multiscale time-step approach, it may be possible to set the same time step for the transient fluid simulation and particle simulation. However, as the time step in fluid simulation becomes infinitesimal, it requires

11

(a)

(b)
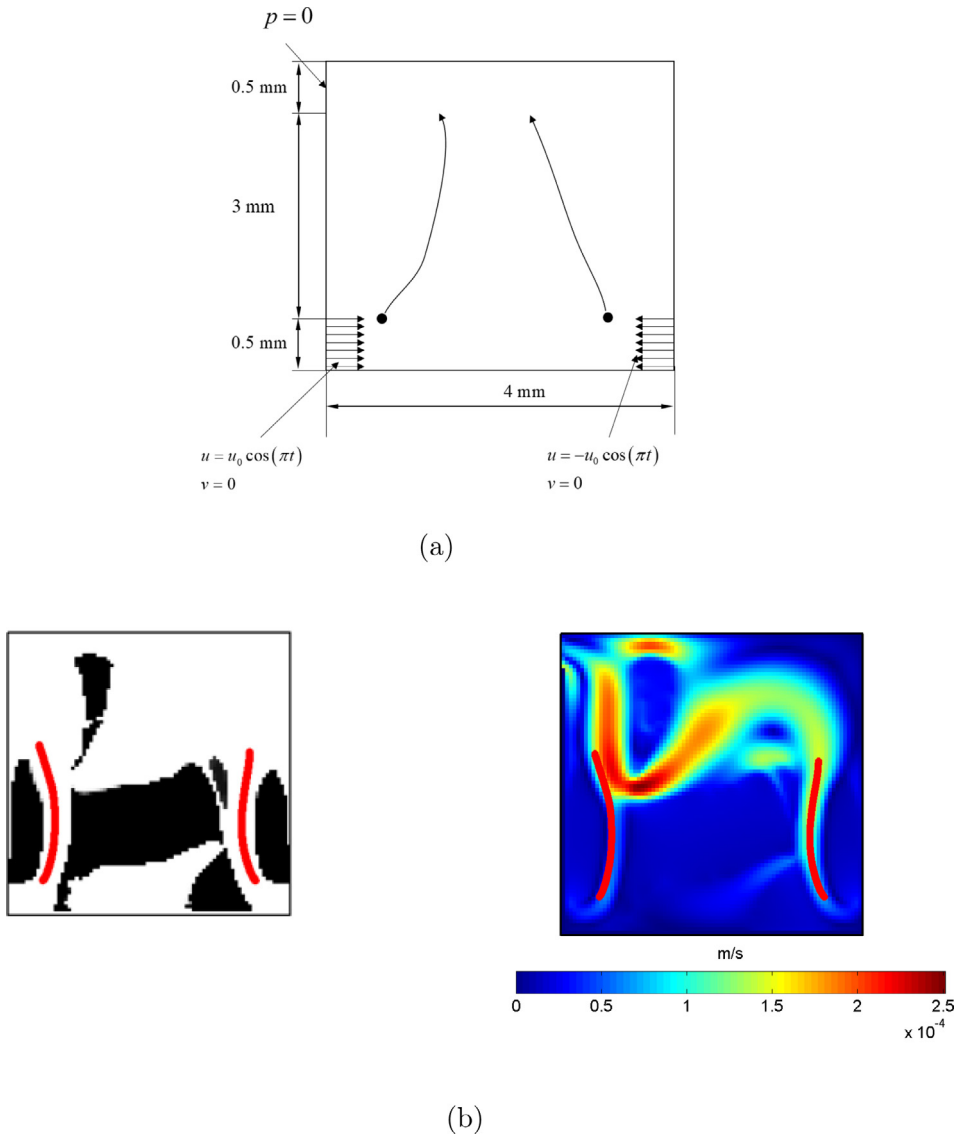
Fig. 9. Example 2: A channel design to move the two particles. (a) Problem definition (initial locations: (0.5, 0.5 mm) and (3.5, 0.5 mm), Fluid : density= 1000 kg/m^3, dynamic viscosity= 1×10^{-3} Pa×s, Particle: mass= 6.367×10^{-11} kg, (Radius =20 μm, density= 1900 kg/m^3, F_D=3.769 $\times 10^{-7}$ $\frac{\text{N·s}}{\text{kg·m}}$, mass$_0$: 30% of the design domain discretized by 80 by 80 quad elements, t_f= 0.5 (s), Δt_f= 0.01 (s), Δt_m= 0.0001 (s)) and (b) the optimized layout with the trajectories of the two particles and its velocity (Red lines: trajectories).

considerable computational time and a convergence issue. Thus, to validate the step, the three different time steps (Δt_f=0.005 s, Δt_f=0.02 s and Δt_f =0.0001 s) are used to obtain the results in Fig. 4. As illustrated, the similar results can be obtained.

It is also an important issue to investigate the effect of the mass constraint and the effect of the mesh refinement. In Fig. 5(a), an optimized layout without a mass constraint is presented. As expected, the nozzle chamber geometry design allows for the effective collection of fluid and smooth movement of fluid and particle. As the particle is centered in the y-direction for 0.1 s in Fig. 5(a) and for 1 s in Fig. 6(a), narrow channels with a void gap along the two center elements were obtained. As the particle moves toward the right side, it turns out that optimized layouts with longer channels can be obtained. With the odd mesh in the y-direction, the particle is located at the centerline

(a)

(b)
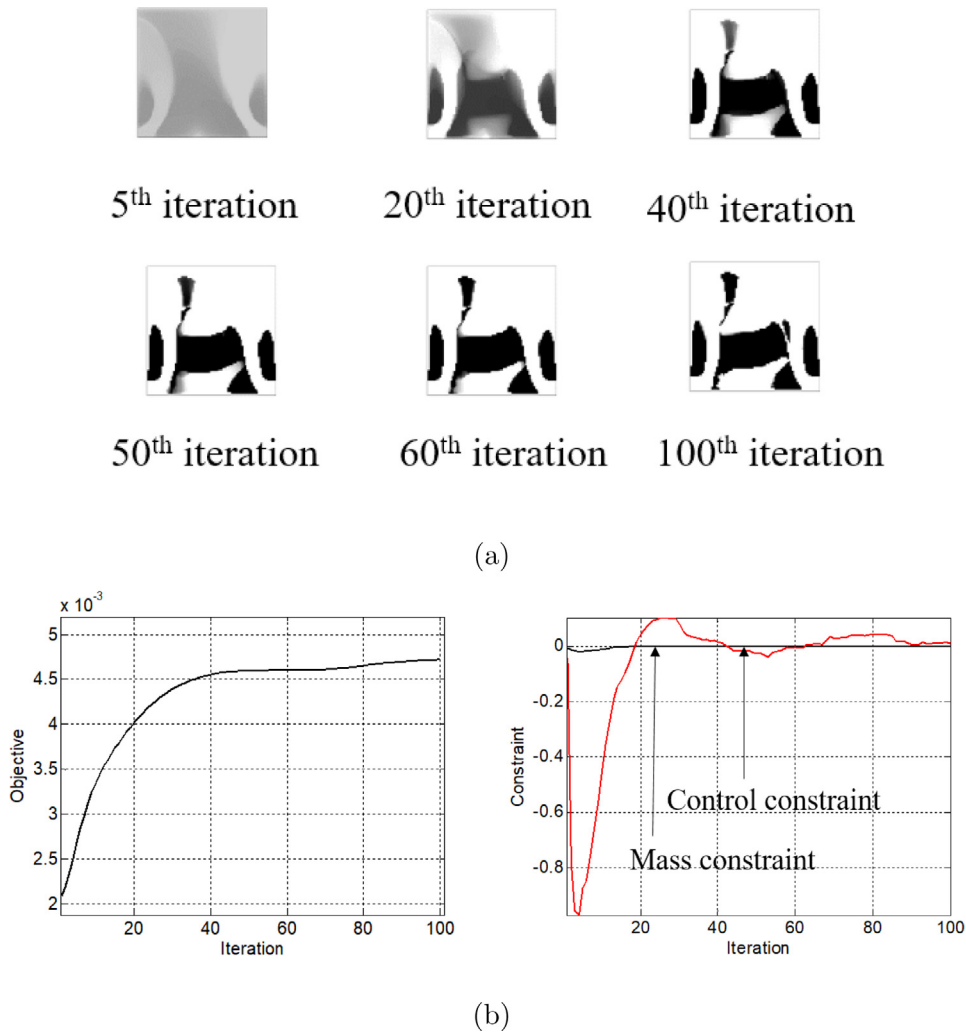
Fig. 10. Intermediate designs and the convergence of the objective and the two constraints.

of the central elements. Thus, the optimized layout shown in Fig. 5(b) and Fig. 6(b) with the center element with a zero design variable (fluid) and the gray adjacent elements can be obtained. These examples show that the present optimization formulation is mesh-dependent. Fig. 7 shows the trajectories of the four designs for 1 s. As the designs with and without the mass constraint are optimized for 0.1 s and 1 s, respectively, their responses are optimized for their specified final times. To test the effect of the boundary conditions, Fig. 8 shows an example with another different boundary condition. In this example, the parabolic flow in the upward direction is assumed to be at the upper boundary condition for 1 s. The optimized layout shown in Fig. 8(b) illustrates that the present optimization framework can provide locally optimized layouts to accelerate the particle.

3.2. Topology optimization example 2: Particle traveling mechanism

For the next example, an optimization problem maximizing the positions of the two identical particles in the y-direction is considered with the mass constraint to improve the optimization process and the position control
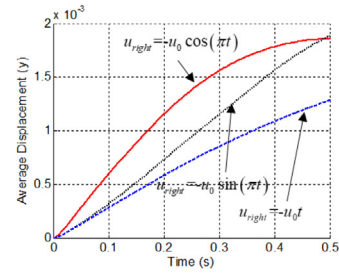
(a) Boundary condition 1: (left: $u = u_0\cos(\pi t)$, right: $u = -u_0\cos(\pi t)$)
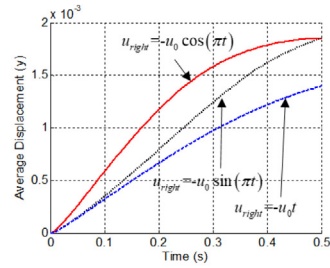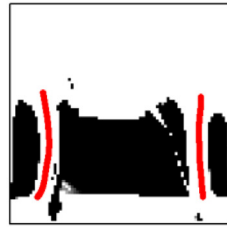
(b) Boundary condition 2: (left: $u = u_0\cos(\pi t)$, right: $u = -u_0\sin(\pi t)$)
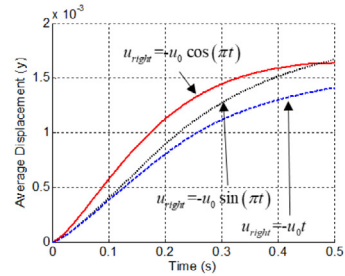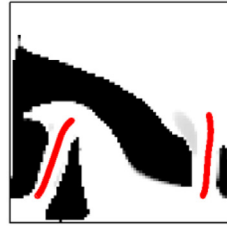
(c) Boundary condition 3: (left: $u = u_0\cos(\pi t)$, right: $u = -u_0 t$)

Fig. 11. Optimization results with the three different boundary conditions. (a) An optimized result with the fluid inputs of the cosine and cosine boundary conditions and the trajectories with the boundary conditions, (b) an optimized result with the fluid inputs of the cosine and sine boundary conditions and the trajectory with the boundary conditions, and (c) an optimized result with the fluid inputs of the cosine and linear boundary conditions and the trajectory with the boundary conditions.

constraint in the y-direction in (23).

$$
\begin{aligned}
&\underset{\boldsymbol{\gamma}}{\text{Max}} \quad p_y^1 + p_y^2 \\
&\text{Subject to Mass} \ \leq \text{mass}_0 \\
&\qquad\qquad (p_y^1 - p_y^2)^2/\epsilon^2 - 1 \leq 0, \quad \epsilon = 10^{-4} \\
&\boldsymbol{\gamma} = [\gamma_1, \gamma_2, \ldots, \gamma_{N_e}], \quad \gamma_{\min} \leqslant \boldsymbol{\gamma} \leqslant 1, \quad \gamma_{\min} = 0.001,
\end{aligned}
\tag{23}
$$

Boundary condition	Design of (a)	Design of (b)	Design of (c)
Boundary condition 1			
Boundary condition 2			
Boundary condition 3			

Fig. 12. Optimization result comparison.

where the y-direction positions of the two particles are denoted by p_y^1 and p_y^2. For 0.5 s, the fluid is inserted through the two inlets along the left and right of the analysis domain, and the time-varying fluid flows toward the upper outlet in Fig. 9. The two particles positioned in the different locations and suspended in the transient fluid follow the streamline of the transient fluid, and the purpose of this optimization problem in (23) is to determine an optimal layout that simultaneously maximizes the average position of the two particles in the y-direction. In addition to the mass constraint regularizing the topology optimization process, the second constraint limiting and equating the y-positions of the particles is also formulated and considered. First, the fluid inputs along the both inlets are assumed to change the magnitudes by $\cos(\pi \times t)$. The detailed geometry is illustrated in Fig. 9(a). With 0.3 for the initial design variables, the optimized layout in Fig. 9(b) is obtained. The two red lines represent the trajectories of the two particles. As the average of the y-positions of the two particles is set to the objective function and is maximized, the optimized layout collecting the fluid flows of the two sides can be obtained to move the particles in the upward direction. It is observed that this optimized design introduces two narrow right and left channels. The fluid magnitudes shown in Fig. 9(b) show that the fluid input inserted at the right inlet initially moves upward and redirects downward in the upper domain. The redirected fluid originating from the right side affects the motion of the left particle to satisfy the second constraint. Fig. 10 shows several intermediate designs and the convergence plots of the objective function and the constraints. The objective value converges monotonically, and the second constraint has some oscillations and fluctuations at the beginning of the optimization iterations. This is because of the complex motion of the particles. Fig. 11(a–c) show the optimization layouts with the different fluid boundary conditions (in (a), left: $u_0\cos(\pi t)$ and right: $-u_0\cos(\pi t)$, in (b), left: $u_0\cos(\pi t)$ and right: $-u_0\sin(\pi t)$, in (c), left: $u_0\cos(\pi t)$ and right: $-u_0 t$). In Fig. 11(a), the optimized layout with the fluid inputs varying with $u_0\cos(\pi t)$ and $-u_0\cos(\pi t)$ is shown. In Fig. 11(b), the optimized layout with the fluid inputs varying with $u_0\cos(\pi t)$ and $-u_0\sin(\pi t)$ is shown. In Fig. 11(c), the optimized layout with the fluid inputs varying with $u_0\cos(\pi t)$ and $-u_0 t$ is shown. Indeed, the different designs optimized for the corresponding boundary conditions were obtained (Fig. 12 and Table 2). Comparing the objective values and the constraints, the designs optimized for the different boundary conditions are better. However, with the better objective functions, the second constraint is violated in the other boundary conditions, as shown in Table 2. As the designs in Fig. 11(a and b) have similar fluid channels, and the objectives and constraints for the second boundary condition are similar. A comparison of the trajectories is shown in Fig. 12 and Table 2.

For the next example, the final time is extended to 1 s in Fig. 9, and the optimized layout shown in Fig. 13, satisfying the second constraint, can be obtained. As the fluid direction is reversed, the particles go up and go down after 0.5 s. This example shows that the present optimization algorithm can be an effective tool for this type of problem.

3.3. Topology optimization example 3: Particle traveling mechanism

For the third example, the topology optimization problem accelerating a particle is considered in (22). The design domain and boundary conditions are shown in Fig. 14. The fluid inputs were prescribed along the upper and bottom

Table 2
Reevaluations of the second optimization design (underline values: the violated constraint for the given boundary condition).
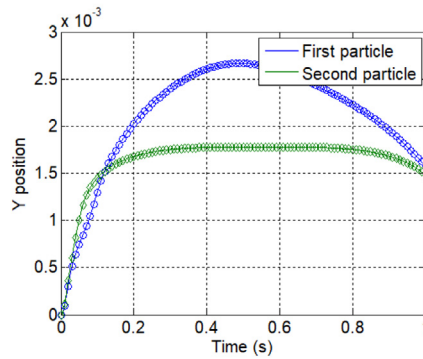
Design	Analysis condition		
	Boundary Condition 1	Boundary Condition 2	Boundary Condition 3
	$(4.7262\times10^{-3}$ m, $8.328\times10^{-3})$	$(4.705\times10^{-3}$ m, $-0.6365)$	$(3.572\times10^{-3}$ m, $\underline{29.64})$
	$(4.777\times10^{-3}$ m, $\underline{15.13})$	$(4.706\times10^{-3}$ m, $-0.5315)$	$(3.798^{-3}$ m, $\underline{24.57})$
	$(4.276\times10^{-3}$, $\underline{109.6})$	$(3.798\times10^{-3}$ m, $\underline{34.253})$	$(3.798\times10^{-3}$ m, $-0.1076)$

(a)
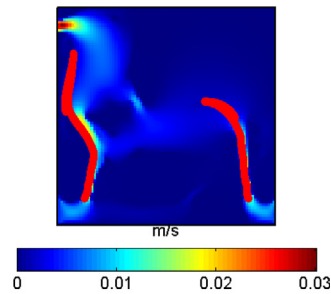
(b)

(c)

Fig. 13. Optimization result with the 1 s final time. (a) Optimized layout, (b) trajectories and fluid velocity, and (c) displacements of the two particles in the *y*-direction.

boundaries. To investigate the effect of the boundary conditions, the two different fluid inputs were considered for the upper and bottom inlets. The magnitudes and final times are varied in the results shown in Figs. 15–18. It seems that the optimized layouts that collect fluid toward the particle can be obtained. The shark pin shape structures optimized for the given conditions can be obtained at the upper and bottom domains. In Table 3, the designs are reevaluated to check whether each design is optimized for the given boundary conditions (see Table 3).

To further investigate the application of this approach, the boundary conditions of this example are changed to $u_{upper} = u_0 \times \cos(2\pi \times t)$ and $u_{lower} = u_0 \times \cos(2\pi \times t + \pi)$ and $t_{\text{final}}=1$ s. Subsequently, the following optimization
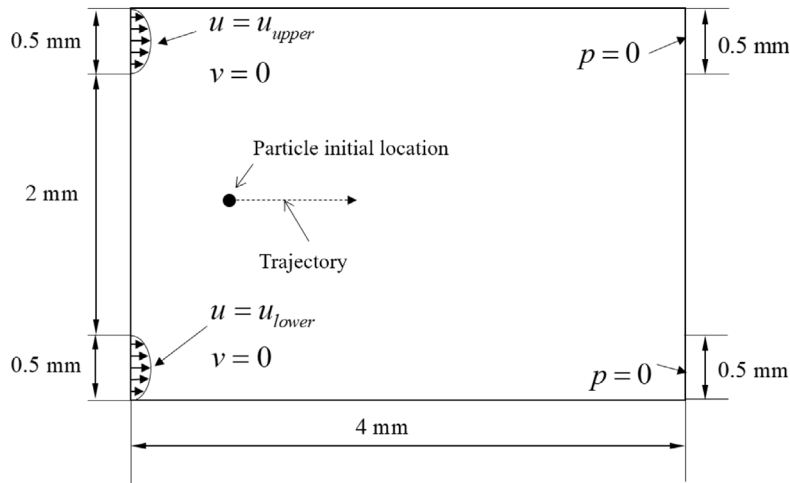
Fig. 14. Example 3: The problem definition for the channel design accelerating particle (Initial location: (1 cm, 1.5 cm), Fluid : density= 1000 kg/m^3, dynamic viscosity= 1×10^{-3} Pa$\times$s, particle: mass= 6.367×10^{-11} kg, (radius =20 µm, density= 1900 kg/m^3, F_D=3.769 $\times 10^{-7} \frac{\text{N} \cdot \text{s}}{\text{kg} \cdot \text{m}}$, mass$_0$: 30% of the design domain discretized by 100 $\times$ 100, t_f= 0.1 and 0.5 (s), Δt_f= 0.01 (s), Δt_m= 5×10^{-6} (s)).

Table 3
Reevaluations of the third optimization designs (The value with * : the best objective function in the analysis conditions).

| Design	Analysis condition			
	(cos, cos, 0.1 (s))	(cos, cos, 0.5 (s))	(sin, sin, 0.1 (s))	(sin, sin, 0.5 (s))
	7.678×10^{-4} m *	1.279×10^{-3} m	2.809×10^{-4} m	1.272×10^{-3} m
	6.426×10^{-4} m	1.279×10^{-3} m *	2.472×10^{-4} m	1.273×10^{-3} m
	6.341×10^{-4} m	1.175×10^{-3} m	2.956×10^{-4} m *	1.167×10^{-3} m
	2.034×10^{-4} m	1.279×10^{-3} m	2.472×10^{-4} m	1.273×10^{-3} m *

result in Fig. 19 is obtained by setting the period of the fluid boundary conditions for the final time. The directions are switched, and the particle moves forward and backward. To maximize the final displacement of the particle in the x-direction, the present optimization algorithm finds out the optimized layout with the empty spaces in the upper and bottom domains with a narrow channel between them.

4. Conclusions

A new topology optimization scheme that considers the interaction between transient fluid and particle is developed. To achieve this, a transient sensitivity analysis for the position of a particle suspended in a fluid is derived. In particular, this research investigates the performance and application of this topology optimization framework in several two-dimensional examples that accelerate particles or control the trajectories of particles. From the examples, the following conclusions can be drawn: First, with the present topology optimization approach, it is now possible to consider the effect of transient motions of particles suspended in a transient laminar flow. By
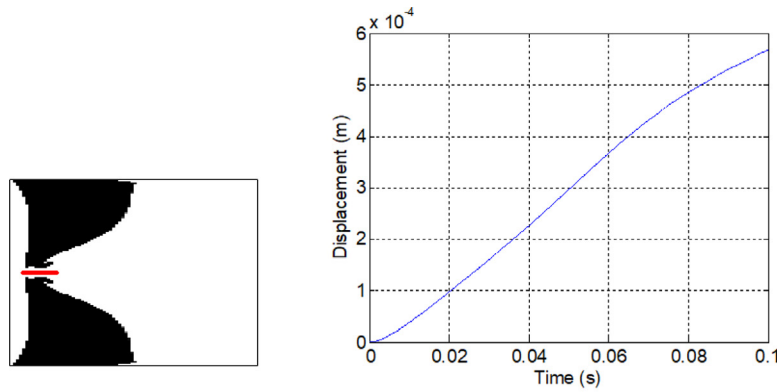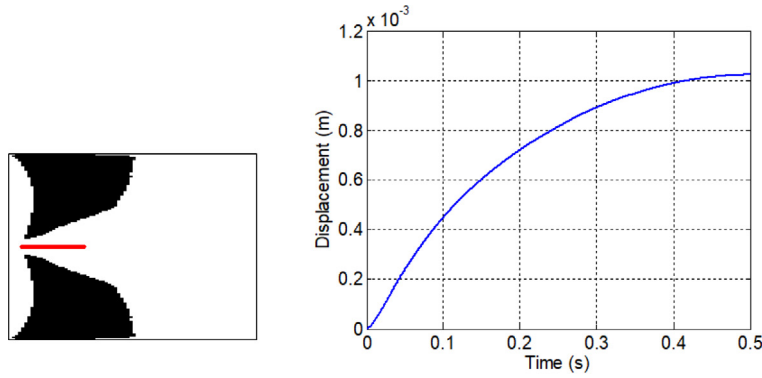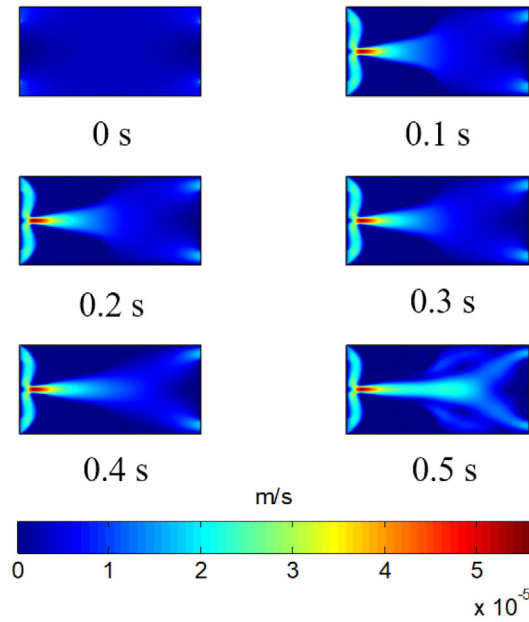
(a)
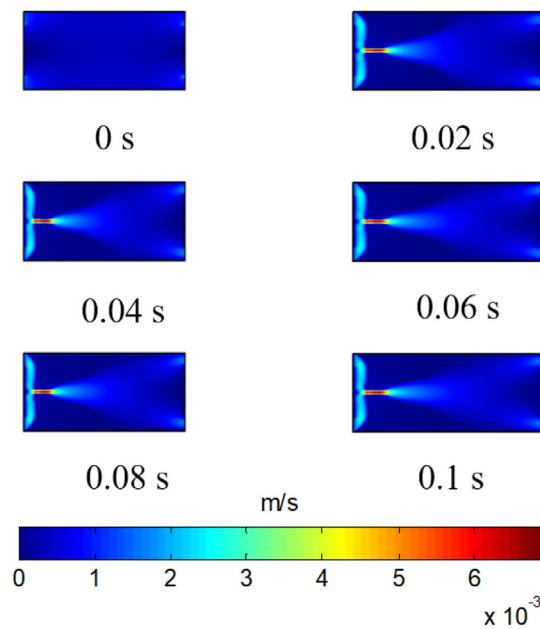
(b)

Fig. 15. Optimization result for 0.1 s with $u_{upper} = u_{lower} = u_0\cos(t \times \pi)$, $u_0 = 0.00125$ m/s. (a) (Left) Optimized layout and (right) trajectory of the particle with respect to time (red lines: trajectory) and (b) flow velocities.

formulating an objective function and constraints with the positions of the particles, the transient trajectories can be controlled by topologically designing the pseudo rigid body. The constraint of the combination of the positions of particles is difficult to be satisfied because the oscillations of positions can cause oscillations of the constraint. The validity of the optimized layouts was investigated with different fluid boundary conditions, and it was found that the topologically optimized layouts minimized the objective function and satisfied the constraints. By changing the boundary condition, a better objective value can be obtained, but the constraint is violated. This implies that the layouts are optimal under the imposed boundary conditions. In addition, for stable and efficient optimization, the
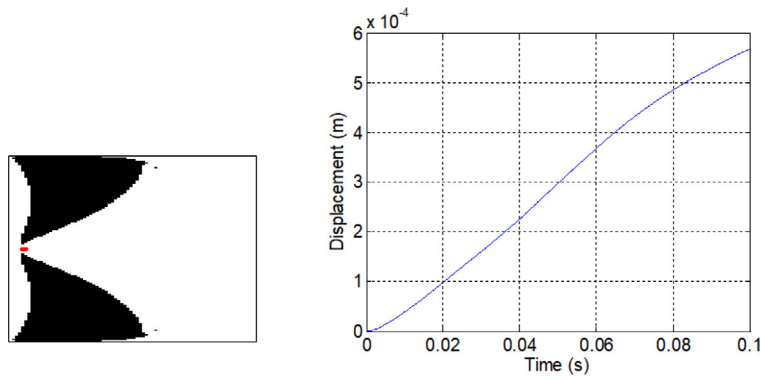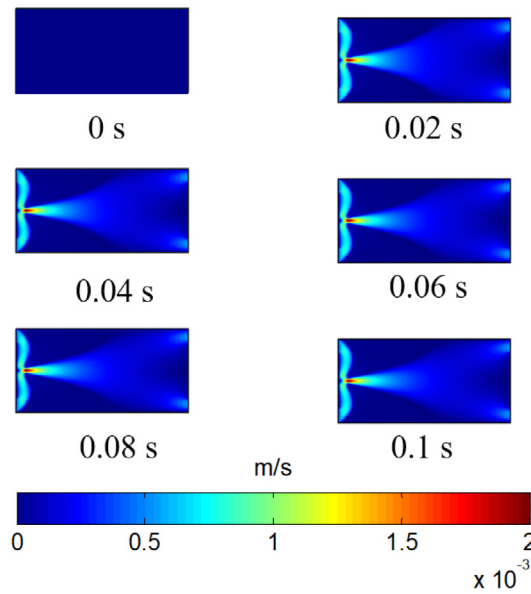
(a)

(b)

Fig. 16. Optimization result for 0.5 s with $u_{upper} = u_{lower} = u_0\cos(t \times \pi)$, $u_0 = 0.00125$ m/s. (a) (Left) Optimized layout and (right) trajectory of the particle with respect to time (red lines: trajectory) and (b) flow velocities.

difference in time scale of the Navier–Stokes equation and the particle equation should be considered. In this study, a two-time scaling approach was presented. Notably, the trajectories of the particles are influenced by the material properties (mass and drag force), fluid velocities, and simulation time. However, similar layouts can be obtained when the trajectories of different particles are similar by adjusting the simulation times. For future research, the consideration of the contact condition of particles is important. In particular, the formulation and its sensitivity analysis considering the contact conditions of particles toward walls or the contact conditions among particles are challenging topics. The application of particle separation devices and/or systems in series is also challenging. In addition, a research considering the effect of the rotational motion of particles is also needed.

(a)

(b)

Fig. 17. Optimization result for 0.1 s with $u_{upper} = u_{lower} = u_0 \sin(t \times \pi)$, $u_0 = 0.00125$ m/s. (a) (Left) Optimized layout and (right) trajectory of the particle with respect to time (red lines: trajectory) and (b) flow velocities.

Declaration of competing interest

The authors declare that they have no known competing financial interests or personal relationships that could have appeared to influence the work reported in this paper.
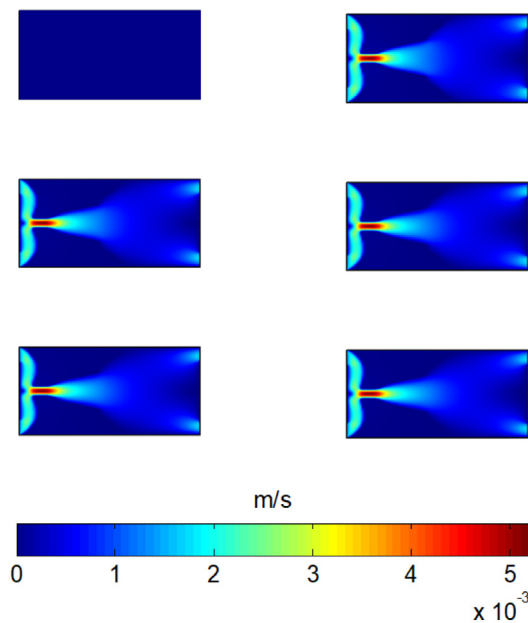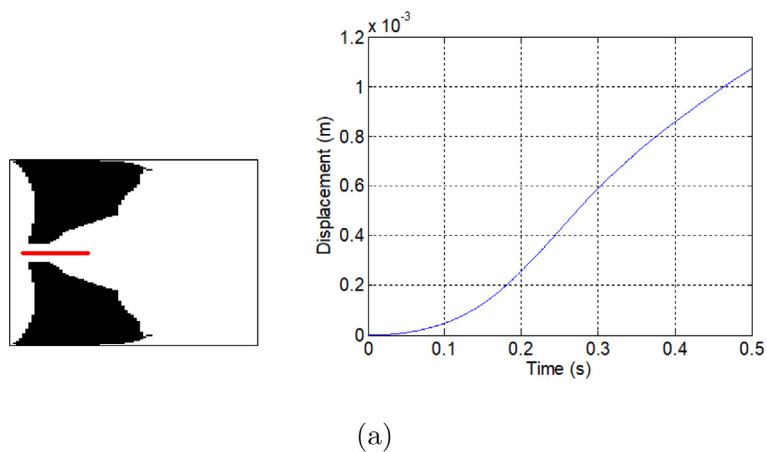
Acknowledgments

(a)

(b)

Fig. 18. Optimization result for 0.5 s with $u_{upper} = u_{lower} = u_0 \sin(t \times \pi)$, $u_0 = 0.00125$ m/s. (a) (Left) Optimized layout and (right) trajectory of the particle with respect to time (red lines: trajectory) and (b) flow velocities.
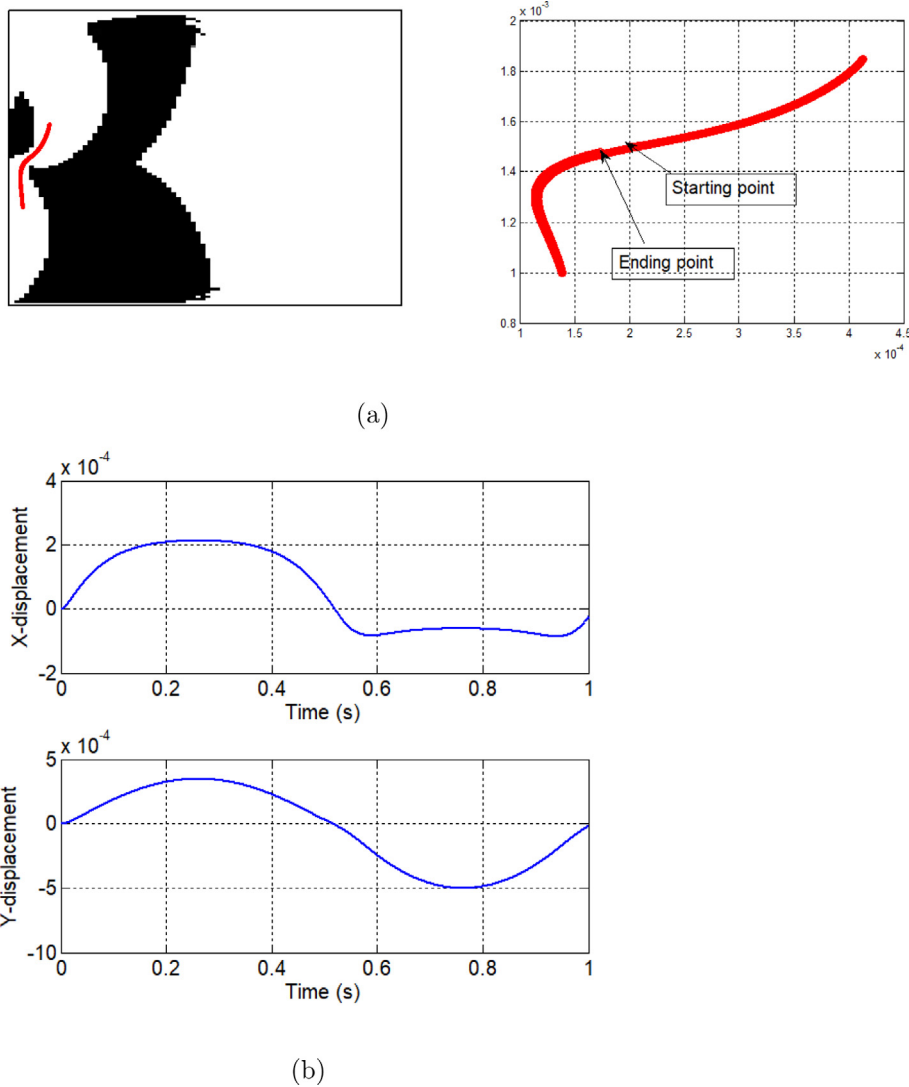
(a)

(b)

Fig. 19. Optimization result for 1 s with $u_{upper} = u_0 \times \cos(2\pi \times t)$, $u_{lower} = u_0 \times \cos(2\pi \times t + \pi)$, $u_0 = 0.0025$ m/s. (a) (Left) Optimized layout and (right) enlarged trajectory of the particle (red lines: trajectory) and (b) trajectories with respect to time.

References

[1] G.H. Yoon, Transient sensitivity analysis and topology optimization for particle motion in steady state laminar fluid, Comput. Methods Appl. Mech. Eng. 367 (2020) 113096.

[2] C.S. Andreasen, A framework for topology optimization of inertial microfluidic particle manipulators, Struct. Multidiscip. Optim. (2020).

[3] G.H. Yoon, H. So, Development of topological optimization schemes controlling the trajectories of multiple particles in fluid, Struct. Multidiscip. Optim. Volume.

[4] M.P. Bendsøe, N. Kikuchi, Generating optimal topologies in structural design using a homogenization method, Comput. Methods Appl. Mech. Eng. 71 (2) (1988) 197–224.

[5] M.Y. Wang, X. Wang, D. Guo, A level set method for structural topology optimization, Comput. Methods Appl. Mech. Eng. 192 (1) (2003) 227–246.

[6] W. Zhang, D. Li, J. Zhou, Z. Du, B. Li, X. Guo, A moving morphable void (MMV)-based explicit approach for topology optimization considering stress constraints, Comput. Methods Appl. Mech. Eng. 334 (2018) 381–413.

[7] V.J. Challis, A discrete level-set topology optimization code written in Matlab, Struct. Multidiscip. Optim. 41 (2010) 453–464.

[8] E.M. Papoutsis-Kiachagias, K.C. Giannakoglou, Continuous adjoint methods for turbulent flows, applied to shape and topology optimization: Industrial applications, Arch. Comput. Methods Eng. 23 (2) (2016) 255–299.

[9] A. Evgrafov, G. Pingen, K. Maute, Topology optimization of fluid domains: Kinetic theory approach, ZAMM - J. Appl. Math. Mech. / Zeitschrift Für Angewandte Mathematik Und Mechanik 88 (2008) 129–141.

[10] K. Yaji, T. Yamada, M. Yoshino, T. Matsumoto, K. Izui, S. Nishiwaki, Topology optimization in thermal-fluid flow using the lattice Boltzmann method, J. Comput. Phys. 307 (2016) 355–377.

[11] Y. Deng, Z. Liu, P. Zhang, Y. Liu, Y. Wu, Topology optimization of unsteady incompressible Navier–Stokes flows, J. Comput. Phys. 230 (17) (2011) 6688–6708.

[12] G.H. Yoon, Topology optimization for turbulent flow with Spalart–Allmaras model, Comput. Methods Appl. Mech. Eng. 303 (2016) 288–311.

[13] G.H. Yoon, Topological design of heat dissipating structure with forced convective heat transfer, J. Mech. Sci. Technol. 24 (6) (2010) 1225–1233.

[14] E.M. Dede, J. Lee, T. Nomura, Multiphysics Simulation: Electromechanical System Applications And Optimization, Springer-Verlag London, 2014.

[15] T. Dbouk, A review about the engineering design of optimal heat transfer systems using topology optimization, Appl. Therm. Eng. 112 (2017) 841–854.

[16] H.S. Damiri, H.K. Bardaweel, Numerical design and optimization of hydraulic resistance and wall shear stress inside pressure-driven microfluidic networks, Lab On A Chip 15 (21) (2015) 4187–4196.

[17] C. Prohm, F. Troltzsch, H. Stark, Optimal control of particle separation in inertial microfluidics, Eur. Phys. J. E 36 (10) (2013) 36–118.

[18] G. Pagano, M. Ventre, M. Iannone, F. Greco, P.L. Maffettone, P.A. Netti, Optimizing design and fabrication of microfluidic devices for cell cultures: An effective approach to control cell microenvironment in three dimensions, Biomicrofluidics 8 (4) (2014) 046503.

[19] H. Bockelmann, V. Heuveline, D.P.J. Barz, Optimization of an electrokinetic mixer for microfluidic applications, Biomicrofluidics 6 (2) (2012) 024123.

[20] H.H. Hu, D.D. Joseph, M.J. Crochet, Direct simulation of fluid particle motions, Theor. Comput. Fluid Dyn. 3 (1992) 285–306.

[21] Y.-C. Wu, B. Yang, An overview of numerical methods for incompressible viscous flow with moving particles, Arch. Comput. Methods Eng. 26 (4) (2019) 1255–1282.

[22] G.H. Yoon, J. Park, Topological design of electrode shapes for dielectrophoresis based devices, J. Electrost. 68 (6) (2010) 475–486.

[23] D. Wang, M. Sigurdson, C.D. Meinhart, Experimental analysis of particle and fluid motion in ac electrokinetics, Exp. Fluids 38 (1) (2005) 1–10, http://dx.doi.org/10.1007/s00348-004-0864-5.

[24] A. Issakhov, R. Bulgakov, Y. Zhandaulet, Numerical simulation of the dynamics of particle motion with different sizes, Eng. Appl. Comput. Fluid Mech. 13 (1) (2019) 1–25.

[25] J.J. Wylie, D.L. Koch, Particle clustering due to hydrodynamic interactions, Phys. Fluids 12 (5) (2000) 964–970.

[26] G.B. Mo, A.S. Sangani, A method for computing Stokes-flow interactions among spherical objects and its application to suspensions of drops and porous particles, Phys. Fluids 6 (5) (1994) 1637–1652.

[27] H. Lee, S. Balachandar, Drag and lift forces on a spherical particle moving on a wall in a shear flow at finite Re, J. Fluid Mech. 657 (2010) 89–125.

[28] J. Zhao, T. Shan, Coupled CFD–DEM simulation of fluid–particle interaction in geomechanics, Powder Technol. 239 (2013) 248–258, http://dx.doi.org/10.1016/j.powtec.2013.02.003, URL https://www.sciencedirect.com/science/article/pii/S0032591013001113.

[29] X.L. Qiu, J.H. Huang, T.M. Westerhof, J.A. Lombardo, K.M. Henrikson, M. Pennell, P.P. Pourfard, E.L. Nelson, P. Nath, J.B. Haun, Microfluidic channel optimization to improve hydrodynamic dissociation of cell aggregates and tissue, Sci. Rep. 8 (2018) 2774.

[30] X.L. Qiu, J. De Jesus, M. Pennell, M. Troiani, J.B. Haun, Microfluidic device for mechanical dissociation of cancer cell aggregates into single cells, Lab On A Chip 15 (1) (2015) 339–350.

[31] A. Dinler, I. Okumus, Inertial particle separation in curved networks: A numerical study, Chem. Eng. Sci. 182 (2018) 119–131.

[32] D. Makhija, G. Pingen, R. Yang, K. Maute, Topology optimization of multi-component flows using a multi-relaxation time lattice Boltzmann method, Comput. & Fluids 67 (2012) 104–114.

[33] P.M. Kulkarni, J.F. Morris, Pair-sphere trajectories in finite-Reynolds-number shear flow, J. Fluid Mech. 596 (2008) 413–435, http://dx.doi.org/10.1017/S0022112007009627.

[34] M.J. Walsh, Influence of particle drag coefficient on particle motion in high-speed flow with typical laser velocimeter applications, Report, NASA, 1976.

[35] G. Bagheri, C. Bonadonna, On the drag of freely falling non-spherical particles, Powder Technol. 301 (2016) 526–544.

[36] K. Svanberg, The method of moving asymptotes – a new method for structural optimization, Int. J. Numer. Methods Eng. 24 (2) (1987) 359–373.

[37] A. Evgrafov, The limits of porous materials in the topology optimization of Stokes flows, Appl. Math. Optim. 52 (3) (2005) 263–277.